Development of Separable Electron Spin Resonance-Computed Tomography Imaging for Multiple Radical Species: An Application to ·OH and ·NO

Ken-ichiro Matsumoto and Hideo Utsumi
Department of Biophysics, Graduate School of Pharmaceutical Sciences, Kyushu University, Higashi-ku, Fukuoka 812-8582, Japan

ABSTRACT A method of separable ESR-CT (electron spin resonance-computed tomography) imaging for multiple radical species was developed and applied to imaging of ·OH and ·NO. The algorithm was improved by combining filtered back-projection with a modified algebraic reconstruction technique to enhance accuracy and shorten calculation time. With this algorithm, spectral-spatial images of the phantom consisting of 3-carbamoyl-2,2,5,5,-tetramethylpyrrolidine-*N*-oxyl and 2-phenyl-4,4,5,5,-tetramethylimidazoline-3-oxide-1-oxyl could be obtained in different directions by rotating the spatial axis. The spatial function of individual radicals was extracted by each of the two methods from each spectral-spatial image. The separative 2D images of each radical were individually constructed using the spatial function obtained with the two methods. By comparing the separative images with the phantom sample, the algorithm for separable ESR-CT imaging was established. This ESR-CT technique was combined with L-band ESR spectroscopy and applied to the separative imaging of ·OH and ·NO, which were spin trapped with 5,5-dimethyl-1-pyrroline-*N*-oxide (DMPO) and Fe^{2+}-*N*-methyl-D-glucamine dithiocarbamate complex, respectively. The ESR signal of DMPO-OH decreased gradually during data acquisition, and the decrease was calibrated by extrapolating the signal intensity to the beginning of data sampling. Both the position and size of the individual images for ·OH and ·NO were in very good agreement with the findings for the sample.

INTRODUCTION

Free radicals such as hydroxyl radical (·OH), superoxide ($\cdot O_2^-$), and nitric oxide (·NO) are very essential and functional compounds in various biological systems. These radicals are independently or sequentially generated in different domains of the bodies of various organisms. Endothelial cells, neutrophils, and macrophages first generate $\cdot O_2^-$ by reducing O_2, which is converted to ·OH through the Fenton reaction, while γ-irradiation produces ·OH directly in cells. ·NO is also produced in endothelial cells, macrophages, and neurocytes, and $\cdot O_2^-$ and ·NO are very rapidly converted into cytotoxic peroxynitrite (Xie and Wolin, 1996), which seems to be associated with apoptotic and/or necrotic cell death (Sandau et al., 1997) and DNA strand breakage (Yoshie and Ohshima, 1997). The interaction of ·NO with H_2O_2, on the other hand, has been suggested to be responsible for DNA damage and cell lysis (Filep et al., 1997). These facts indicate that the interactions among radical species have a large influence on their function in physiological and pathological phenomena. The interactions among radical species largely depend on both the amount and location of radicals generated. Therefore, the detection and simultaneous mapping of individual radical species generated in vivo are both essential for understanding the function of radical formation in vivo.

In vivo ESR spectroscopy is very useful for understanding the redox reactions in physiological phenomena (Takeshita et al., 1993, 1999; Gomi et al., 1993) and in oxidative injuries, such as ischemia-reperfusion (Masuda et al., 1992; Utsumi et al., 1993), hypoxia-hyperoxia (Miura et al., 1992, 1995), streptozotocin-induced diabetes (Sano et al., 1998), iron overload (Phumala et al., 1999), and selenium deficiency (Matsumoto et al., 2000). The combination of in vivo ESR spectroscopy with an imaging technique allows 2D or 3D imaging of radicals in living organisms (Takeshita et al., 1991; Sano et al., 1997, 2000). Most conventional ESR-CT techniques utilize deconvolution of a spectrum under a field gradient with that under zero field gradient to obtain spatial projection (Hoch, 1981; Ohno, 1982; Sotgiu et al., 1987). Fourier transformation (FT) deconvolution is only applicable to samples composed of a single radical species. Samples having more than two radical species produce a nonsense image by ESR-CT using FT deconvolution. However, it often happens that multiple radical species are produced and coexist in biological systems. Therefore, to understand the role of free radical reactions in pathological and physiological phenomena, there is need for an ESR-CT technique in which individual radical species can be separately visualized within an organ.

For the separable ESR-CT technique to be effective, it is essential that the spatial function of each radical be separately obtained. Such separation of the spatial function of individual radicals can be achieved by utilizing three techniques: the localized ESR technique (Katsuda et al., 1990), the modulated field gradient technique (Herrling et al., 1982), and the spectral-spatial imaging technique (Ewert

Received for publication 17 August 1999 and in final form 24 August 2000.

Address reprint requests to Dr. Hideo Utsumi, Department of Biophysics, Graduate School of Pharmaceutical Sciences, Kyushu University, Higashi-ku, Fukuoka 812-8582, Japan. Tel.: 81-92-642-6621; Fax: 81-92-642-6626; E-mail: utsumi@pch.phar.kyushu-u.ac.jp.

Dr. Matsumoto's present address is Showa Pharmaceutical University, Higashi-Tamagawagakuen, Machida, Tokyo 194-8543, Japan.

0006-3495/00/12/3341/09 $2.00

and Herrling, 1986; Maltempo, 1986; Maltempo et al., 1987, 1988). The spectral-spatial imaging technique has been developed within the field of NMR spectroscopy (Lauterbur et al., 1984; Bernardo et al., 1985) and has the distinct advantage that it requires no special devices other than those used for ESR-CT itself. Eaton et al. (1987) and Sueki et al. (1990) first reported the possibility of using the spectral-spatial imaging technique for separable ESR-CT imaging of multiple radical species. They obtained 3D spectral-spatial images of phantom samples consisting of stable radicals such as 1,1-diphenyl-2-picrylhydrazyl (DPPH) and/or 4-oxo-2,2,6,6-tetramethylpyperidine-*N*-oxyl (TEMPONE), using X-band ESR spectroscopy and high field gradient coils (400 Gauss/cm) (Eaton et al., 1987), and succeeded in 2D spatial-spatial imaging of the signal intensities from the 3D spectral-spatial imaging, using the same system (Sueki et al., 1990). However, no separable ESR-CT imaging of multiple radical species has been reported in either in vitro or in vivo experiments.

The spectral-spatial imaging technique requires a very high field gradient and therefore leads to a lack of projection data within the missing angle (Maltempo, 1986; Maltempo et al., 1991). In the use of ESC-CT in vivo, it is very important that the field gradient be reduced and that the data acquisition be shortened. In vivo ESR measurement requires a wide resonator, which creates a large distance between the field gradient coils and small field gradient. The projection number must be limited because of the short acquisition time for in vivo ESR imaging data. The half-life of the ESR signal of a stable nitroxyl radical is around 10–15 min, and at least 5–10 s is needed to obtain one spectrum for an in vivo ESR measurement because of the reduced signal-to-noise ratio. Thus, the projection number is calculated to be 60–180, resulting in a wide missing angle and an insufficient number of projections.

Kuppusamy et al. (Kuppusamy and Zweier, 1995; Kuppusamy et al., 1994, 1995) have succeeded in imaging oxygen concentrations in the isolated rat heart. They estimated the line width from 3D and/or 4D spectral-spatial images, which were reconstructed from 144 projections, using a 25-mm resonator and 10–100-Gauss/cm field gradient. Their data acquisition times were 16 min for 3D and 104 min for 4D spectral-spatial images, respectively. However, their spectral width was only 3.5 G, because they estimated the line width with only one resonance line. A much wider spectral width (e.g., 50 G) is required for separable ESR-CT imaging of multiple radicals, and such a width leads to a much wider missing angle and fewer projections.

In addition to these problems, it is important to pay attention to the signal decay of each radical species in the separable ESR-CT imaging for multiple radical species, because the individual radical species have a corresponding signal decay rate. The different signal decay of individual radicals causes imaging distortion after data acquisition. The signal decay thus should be normalized by the use of an adequate algorithm.

The imaging of two radical species in particular, ·OH and ·NO, is highly important in in vivo free radical studies, because these are the key radical species of the in vivo free radical reaction. The purpose of the present work was to develop an algorithm for separable ESR-CT imaging based on the spectral-spatial imaging technique and to apply this separable ESR-CT imaging technique to the biologically important radical species ·OH and ·NO. In this experiment, we used only 29 or 13 projections for spectral-spatial imaging within ±70° or ±72°. Both problems, the reduction in number of projection and the signal decay during the acquisition time, are discussed.

MATERIALS AND METHODS

Materials

3-Carbamoyl-2,2,5,5,-tetramethylpyrrolidine-*N*-oxyl (carbamoyl-PROXYL), ferrous sulfate, and H_2O_2 were purchased from Aldrich Chemical Co., Inc. (Milwaukee, WI), Ishizu Pharmaceutical Co., Ltd. (Osaka, Japan), and Wako Pure Chemical Industries, Ltd. (Osaka, Japan), respectively. 5,5-Dimethyl-1-pyrroline-*N*-oxide (DMPO) and 2-phenyl-4,4,5,5,-tetramethylimidazoline-3-oxide-1-oxyl (PTIO) were from LABOTEC Co. (Tokyo, Japan). *N*-Methyl-D-glucamine dithiocarbamate (MGD) was synthesized in our laboratory by the method of Sinobu et al. (1984).

Carbamoyl-PROXYL and PTIO were dissolved in distilled water at 0.5 and 5.0 mM, respectively. Fe^{2+}-MGD complex was prepared by mixing the solutions of ferrous sulfate (76.5 mM, 0.5 ml) and MGD (382.5 mM, 1.0 ml), and then ·NO gas (Nihon-Sanso, Fukuoka, Japan) was bubbled through the Fe^{2+}-MGD complex solution to prepare Fe^{2+}-MGD-NO complex as described by Lai and Komarov (1994). ·OH was prepared by the Fenton reaction and trapped with DMPO to form DMPO-OH.

Separable ESR-CT

The data for spectral-spatial images at different spatial axes were obtained as described by Maltempo et al. (1987) with an X-band or L-band ESR spectrometer (JES-RE3X or JES-RE3L; JEOL, Tokyo, Japan) equipped with three-dimensional field gradient coils and rapid scan coils. Control of the field gradient coils and data acquisition were performed with a personal computer. ESR measurement was done at 0.1–0.16 mT with a field modulation of 100 kHz and 2–10 mW at microwave frequency (1.22 or 9.42 GHz).

Thirteen or 29 projections were obtained within the angle ranges of either ±72° or ±70° for each spectral-spatial image. The spectral-spatial image (5.0 mT × 50.0 mm or 6.0 mT × 60.0 mm, 128 × 128 image matrix) was first constructed by filtered back-projection (FBP), using a Shepp-Logan filter (Shepp and Logan, 1974). The initial image obtained by FBP was corrected using the algebraic reconstruction technique (ART), which was modified by calibrating the pixel density and area in the additive correction (mART). The corrected image was then corrected twice more by mART. The details of the mART are described in the Discussion.

Spatial projection of radical distribution was obtained from the four or six spectral-spatial images by rotating the spatial axis as described in the Results. With the resulting four or six spatial projections, the secondary 2D spatial images of the individual radical species were reconstructed by the combination of FBP and three corrections by mART.

RESULTS

Development of algorithm for separable ESR-CT imaging

Two radicals, carbamoyl-PROXYL and PTIO, were used as a phantom to develop the algorithm for separable ESR-CT imaging. Carbamoyl-PROXYL is a water-soluble nitroxyl radical that is widely used for estimation of in vivo free radical reactions and in vivo imaging (Berliner and Wan, 1989; Alecci et al., 1990; Utsumi et al., 1990, 1993; Ishida et al., 1992; Sano et al., 1998; Phumala et al., 1999; Matsumoto et al., 2000), while PTIO is reactive toward ·NO and is used as a scavenger for ·NO (Akaike et al., 1993). Fig. 1, *A* and *B*, shows the X-band ESR spectra of PTIO and carbamoyl-PROXYL without field gradient, respectively. An aqueous solution of PTIO and carbamoyl-PROXYL gave quintuplet lines (hfs = 0.77 mT, peak height ratio = 1:2:3:2:1) and triplet lines (hfs = 1.52 mT, peak height ratio = 1:1:1), respectively. Fig. 1 *C* shows the spectrum of the phantom composed of both radicals, which is illustrated in Fig. 1 *D*. All lines other than the second and the fourth of the PTIO signal were overlapped with that of carbamoyl-PROXYL.

The four spectral-spatial images were obtained along different spatial axes, as shown in Fig. 1 *D*. The calculation for the spectral-spatial image was performed in three different ways—using FBP only, using mART only, or using a combination of FBP with mART. The calculation periods required for FBP and one iteration of the mART correction were 10–15 s and 3–5 min in the case of 12–18 projections created with a computer and a 300-MHz clock. When mART correction only was used, at least 10 iterations of correction were needed to reconstruct a satisfactory image. Thus the total estimated time for all procedures involving spectral-spatial images and separative ESR-CT should be on the order of several hours. The combination of FRP with one iteration of mART correction yielded an image of approximately the same quality as that given by 10 iterations of mART only (data not shown). Therefore, to shorten the calculation time, FBP was adopted for construction of the first image for mART correction.

Fig. 2 demonstrates the spectral-spatial image along the 135° axis obtained with the combination of FBP with mART. As can be seen, the signals of carbamoyl-PROXYL and PTIO are separately distinguishable. The dotted line marked s_1 in the upper part of the spectral-spatial image corresponds to the first line of carbamoyl-PROXYL at the spatial position s_1, and the solid line marked s_2 corresponds to the first and second lines of PTIO at s_2. Points *a* and *b* indicate the tops of the first line of carbamoyl-PROXYL and the second line of PTIO, respectively. The spatial function of each radical along the four spatial axes was obtained from the corresponding spectral-spatial images by the following two methods.

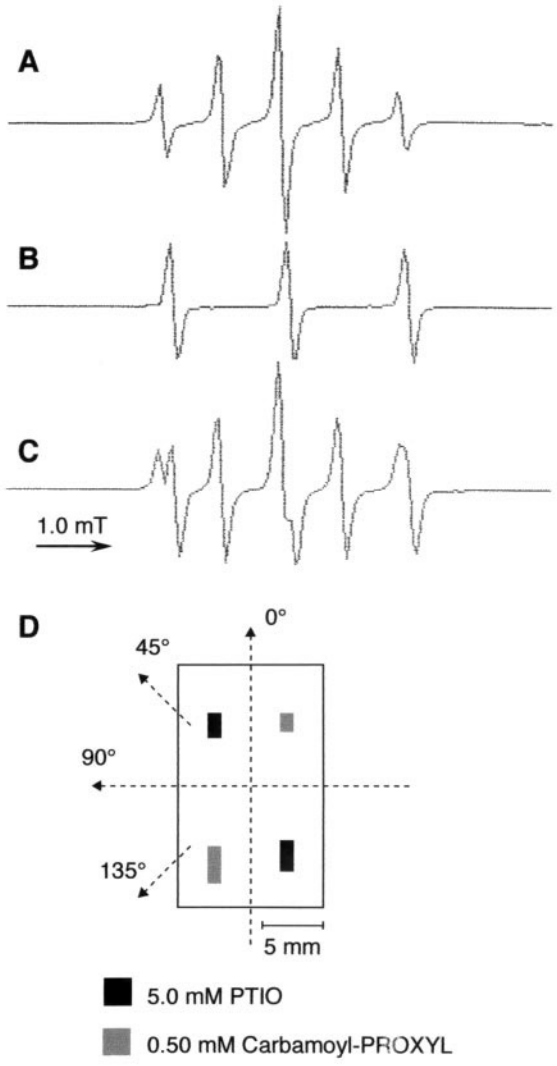

FIGURE 1 X-band ESR spectra of radicals used for the phantom. The phantom (*D*) was prepared with an aqueous solution of 5.0 mM PTIO and 0.5 mM carbamoyl-PROXYL. ESR spectra of the 5.0 mM aqueous solution of PTIO (*A*), the 0.50 mM aqueous solution of carbamoyl-PROXYL (*B*), and the phantom containing both radicals (*C*) were obtained at 10 mW of 9.4 GHz microwave and 0.1 mT of 100 kHz field modulation. The rectangle in *D* indicates the range of ESR-CT image reconstruction (20 mm × 12 mm).

Method 1

The peak height at the point *b* of the spectral axis in Fig. 2 corresponds to the amount of PTIO, indicating that the signal intensity at point *b* along the spatial axis, indicated by P_b in the right panel of Fig. 2, must be the one-dimensional spatial projection of PTIO. On the other hand, the signal intensity at point *a* (shown with P_a) includes not only the intensity of carbamoyl-PROXYL, but also a small amount of the superimposed PTIO. In this case, the contamination of PTIO at point *a* was calculated to be 0.095. Therefore, the

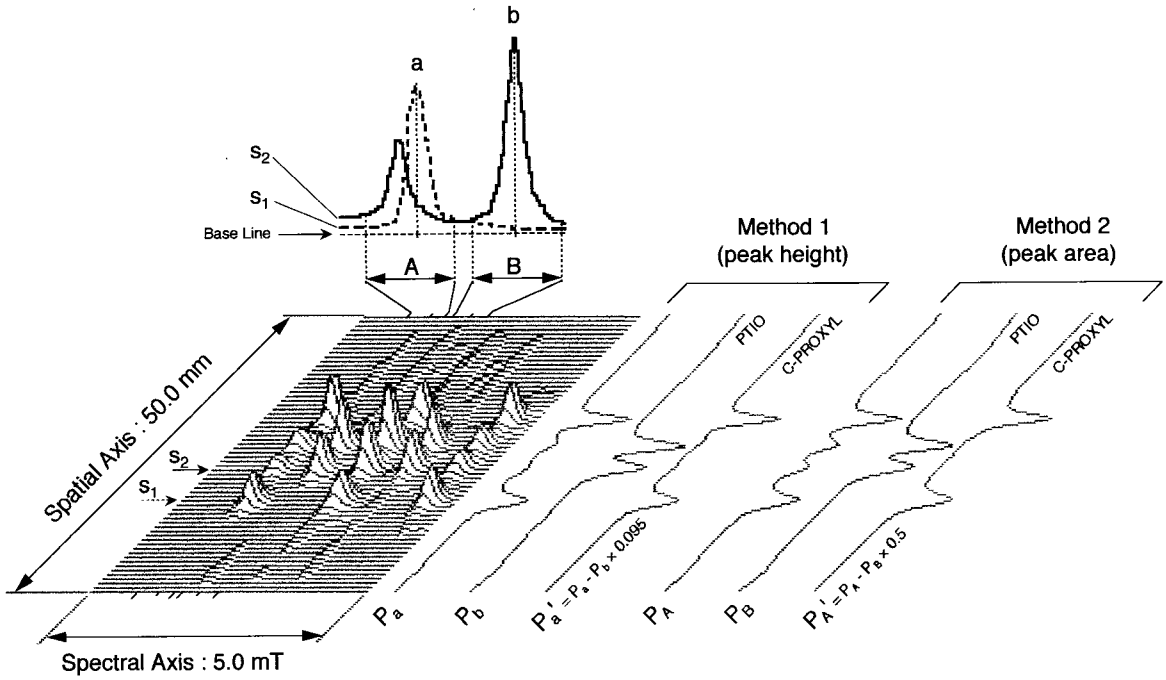

FIGURE 2 Spectral-spatial image and one-dimensional spatial function of the phantom composed of PTIO and carbamoyl PROXYL. The spectral-spatial image was obtained in the 135° direction of the phantom shown in Fig. 1 *D*. The spectral-spatial image was reconstructed on a 128 × 128 image matrix corresponding to the 5.0 mT × 5.0 cm spectral-spatial plane, with 29 projections obtained, using ±2.75 mT/cm as the maximum field gradient. The dotted line marked s_1 in the upper part of the spectral-spatial image corresponds to the first line of carbamoyl-PROXYL at the spatial position s_1, and the solid line marked s_2 corresponds to the first and second lines of PTIO at s_2. Points *a* and *b* indicate the top of the first line of carbamoyl-PROXYL and the second line of PTIO, respectively. The ranges *A* and *B* are the spectral width covering the first line of both radical species and the second line of PTIO, respectively. The one-dimensional spatial projections, P_a, P_b, $P_{a'}$ ($= P_a - P_b \times 0.095$), P_A, P_B, and $P_{A'}$ ($= P_A - P_B \times 0.5$) were obtained as described in the text.

spatial projection of carbamoyl-PROXYL (indicated by $P_{a'}$ in Fig. 2, *right*) was obtained as $P_a - (P_b \times 0.095)$.

Method 2

The concentrations of the two radicals were calculated from the peak area in the ranges of *A* and *B* at the spectral axis in Fig. 2. The spatial projection P_B, which was the peak area within *B* along the spatial axis, was used as the spatial projection of PTIO. The peak area within *A* contributed one-third of the amount of carbamoyl-PROXYL and one-ninth of the amount of PTIO. Thus, the spatial projection of carbamoyl-PROXYL ($P_{A'}$) was obtained by subtracting half of P_B from P_A, because the signal intensity of PTIO in the lowest field was half of the second line of PTIO.

Next, the separative ESR-CT images of two radicals, PTIO and carbamoyl-PROXYL, were independently reconstructed from the corresponding spatial projection along four spatial axes. Fig. 3, *A* and *B*, are the spatial-spatial images of PTIO and carbamoyl-PROXYL, respectively, which were reconstructed from the spatial projection obtained by method 1, and Fig. 3, *C* and *D*, are those obtained by method 2. The position and scale of the PTIO images in Fig. 3 showed good agreement with those of the phantom. However, the image of carbamoyl-PROXYL by method 1 (Fig. 3 *B*) was contaminated with the image of PTIO, probably because of incomplete subtraction by method 1. In contrast, the image of carbamoyl-PROXYL by method 2 (Fig. 3 *D*) was in very good agreement with that of the phantom. These results indicate that method 2 utilizing the peak area is highly reliable for obtaining spatial projection.

Separative imaging of ·NO with ·OH

The L-band ESR spectra of DMPO-OH and Fe^{2+}-MGD-NO without field gradient are shown in Fig. 4, *A* and *B*, respectively. An aqueous solution of DMPO-OH gave quartet lines ($g = 2.007$, hfs = 1.50 mT, peak height ratio = 1:2:2:1, line width = 0.2 mT), and Fe^{2+}-MGD-NO gave triplet lines ($g = 2.04$, hfs = 1.25 mT, peak height ratio = 1:1:1, line width = 0.3 mT). The phantom containing both spin adducts was prepared as shown in Fig. 4 *D*, and Fig. 4 *C* demonstrates the spectrum of the phantom. The second and third lines of both adducts were completely superimposed, while the first lines of DMPO-OH and Fe^{2+}-MGD-NO were partially overlapped.

Six spectral-spatial images were obtained by rotating the spatial axis as shown in Fig. 4 *D*. Fig. 5 shows the spectral-

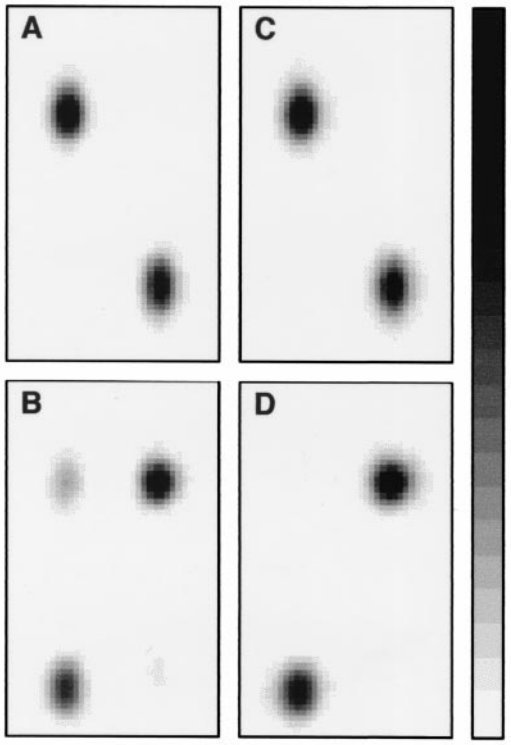

FIGURE 3 Separative ESR-CT images of PTIO (*A* and *C*) and of carbamoyl-PROXYL (*B* and *D*). Images *A* and *B* were constructed with a spatial projection obtained by method 1, and images *C* and *D* were constructed with a projection obtained by method 2. Each image was reconstructed within the range of 20 mm × 12 mm of the spatial-spatial plane.

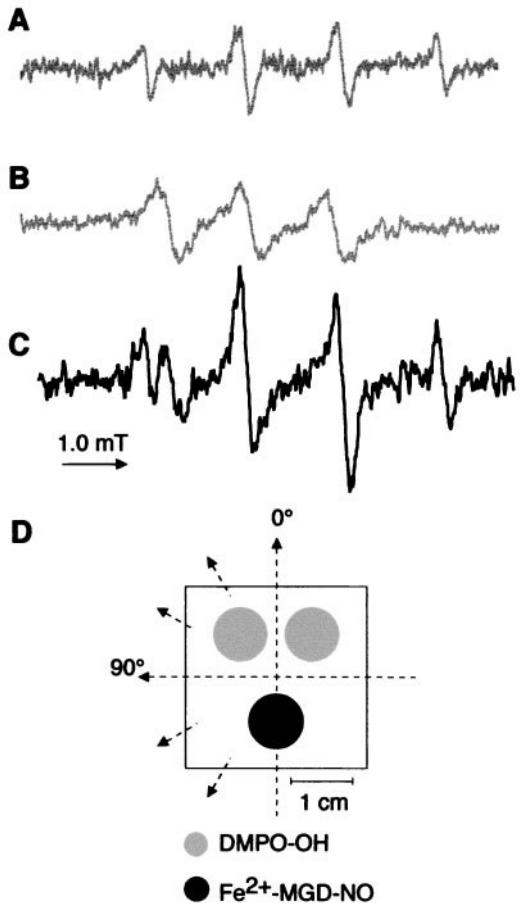

FIGURE 4 L-band ESR spectra of radicals used for the phantom. The phantom (*D*) was prepared with an aqueous solution of DMPO-OH and Fe^{2+}-MGD-NO in the tubes (i.d. = 9 mm). ESR spectra of the aqueous solution of DMPO-OH (*A*), the aqueous solution of Fe^{2+}-MGD-NO (*B*), and the phantom containing both spin adducts (*C*) were obtained at 5 mW of 1.1 GHz microwave and 0.1 mT of 100 kHz field modulation. The square in *D* indicates the range of the ESR-CT image reconstruction (30 mm × 30 mm).

spatial image in the 0° direction. The triplet and the quartet lines are clearly distinguished at the different spatial positions. Hyperfine splitting of the quartet and triplet lines in the spectral-spatial image was 1.25 mT and 1.50 mT, respectively, which agreed well with the conventional spectra of DMPO-OH and Fe^{2+}-MGD-NO shown in Fig. 4, *A* and *B*, respectively. The line widths of the quartet and triplet lines in the spectral-spatial images also agreed with those of conventional spectra.

One-dimensional spatial projection of DMPO-OH (shown as P_B in Fig. 5, *right*) was obtained from the peak area in the range *B* of the fourth line of the DMPO-OH signal. The spatial projection of Fe^{2+}-MGD-NO ($P_{A'}$) was obtained by subtracting the superimposed DMPO-OH (precisely the spatial profile P_B) from the spatial profile P_A in the range *A* of Fig. 5, which contained the first lines of the DMPO-OH and Fe^{2+}-MGD-NO signals.

During data acquisition, the ESR signal of DMPO-OH decreased gradually, while that of Fe^{2+}-MGD-NO was very stable (Fig. 6). The decrease in the signal intensity of DMPO-OH was calibrated by extrapolating the signal intensity to the beginning of data acquisition. The spatial-spatial images of the two adducts, DMPO-OH and Fe^{2+}-MGD-NO, were independently reconstructed (Fig. 7, *A* and *B*, respectively). The position and scale of the reconstructed images of DMPO-OH and Fe^{2+}-MGD-NO were well fitted to those of the phantom shown in Fig. 4 *D*.

DISCUSSION

In this experiment, we developed an algorithm for separable-ESR-CT imaging of multiple radical species by combining the 2D spectral-spatial imaging technique with the 2D spatial imaging technique and succeeded in the separative imaging of ·OH and ·NO, both of which are thought to be key radical species of in vivo free radical reactions.

A number of previous studies have provided 2D or 3D images of radicals in living animals (Berliner and Wan, 1989; Alecci et al., 1990; Takeshita et al., 1991; Ishida et

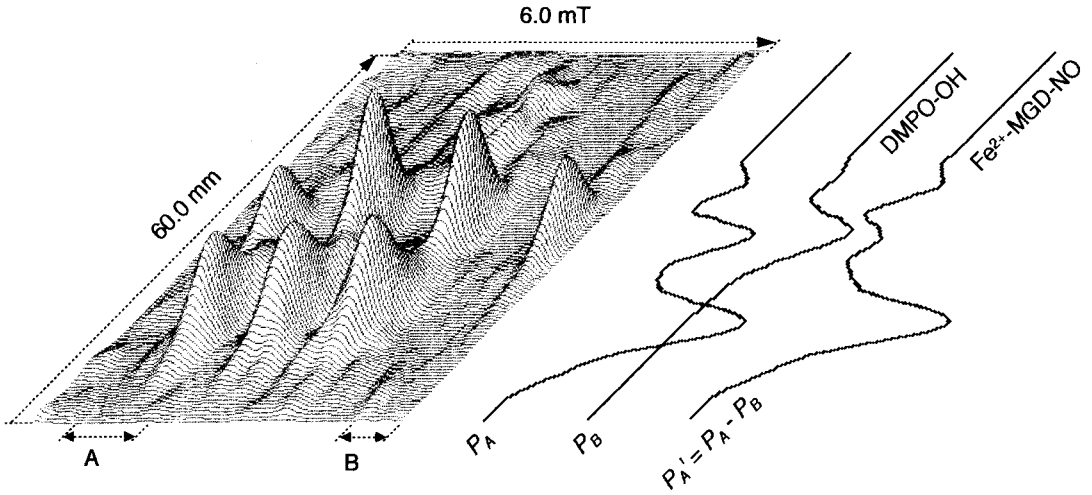

FIGURE 5 Spectral-spatial image and one-dimensional spatial function of the phantom composed of DMPO-OH and Fe^{2+}-MGD-NO. The spectral-spatial image in the 0° direction in Fig. 4 *D* was reconstructed on a 128 × 128 image matrix corresponding to a 6.0 mT × 6.0 cm spectral-spatial plane with 13 projections obtained using ±3.08 mT/cm as the maximum field gradient. The spatial projections, P_A, P_B, and $P_{A'}$ ($= P_A - P_B$), were obtained as described in the text.

al., 1992; Sano et al., 1997, 2000; Yokoyama et al., 1997). In these reports, exogenous nitroxyl radicals or iron complexes of ·NO generated in vivo were visualized using the CW ESR-CT technique. In those experiments Fourier deconvolution was used to calculate the spatial function, but that approach is not applicable for a sample containing multiple radical species. A new technique must therefore be developed for separable ESR-CT imaging.

In the present paper, we utilized a 2D spectral-spatial imaging technique for in vivo separable-ESR-CT imaging of multiple radical species, the principle of which was first proposed by Eaton and colleagues (Eaton et al., 1987; Sueki et al., 1990). Kuppusamy et al. (Kuppusamy and Zweier, 1995; Kuppusamy et al., 1994, 1995b) have also succeeded in imaging the oxygen concentration of the isolated rat heart. However, no separable ESR-CT imaging for multiple radical species has been reported in either in vitro or in vivo experiments. The usual spectral-spatial imaging technique requires a very high field gradient, leading to an absence of projection data within the missing angle (Maltempo, 1986; Maltempo et al., 1991). And wider spectral width is required for the separable ESR-CT imaging of multiple radicals, leading to a much wider missing angle and even fewer projections. It is quite essential for in vivo separable ESR-CT to reduce the field gradient and shorten the data acquisition. In addition, it is important to address the signal decay of each radical species in the separable ESR-CT imaging for multiple radical species, because the individual radical species have the corresponding signal decay rate. We therefore improved the algorithm for 2D spectral-spatial imaging such that it would be applicable to in vivo separable ESR-CT imaging for multiple radical species.

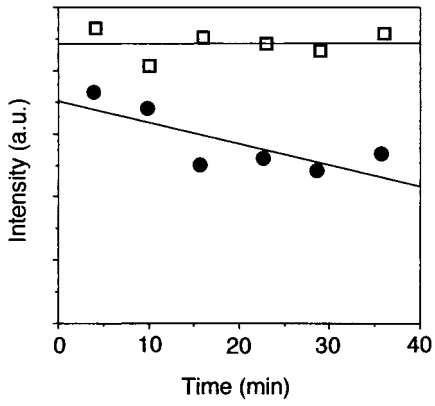

FIGURE 6 Signal decays of DMPO-OH and Fe^{2+}-MGD-NO during data acquisition. The logarithms of the signal intensities of DMPO-OH (●) and Fe^{2+}-MGD-NO (□) were plotted against time after the beginning of acquisition. The signal intensity of DMPO-OH was obtained from the peak area of the fourth line (independent peak of DMPO-OH) of the spectrum without field gradient, and that of Fe^{2+}-MGD-NO was obtained by subtracting the overlapped DMPO-OH signal from the peak area of the first line (partly superimposed DMPO-OH and Fe^{2+}-MGD-NO).

Although FBP has the advantage of reconstructing an accurate image within a short calculation time, it also results in an insufficient quantity of projection data and produces an image with severe star artifacts and noise (Woods et al., 1991). In contrast, ART requires a longer calculation time because of iterative algorithms, but the reduction in projections has less effect on the image accuracy (Gordon et al., 1970). There are two types of ART algorithm, those employing additive and those employing multiplicative corrections (Gordon and Herman, 1974; Brooks and Chiro, 1975).

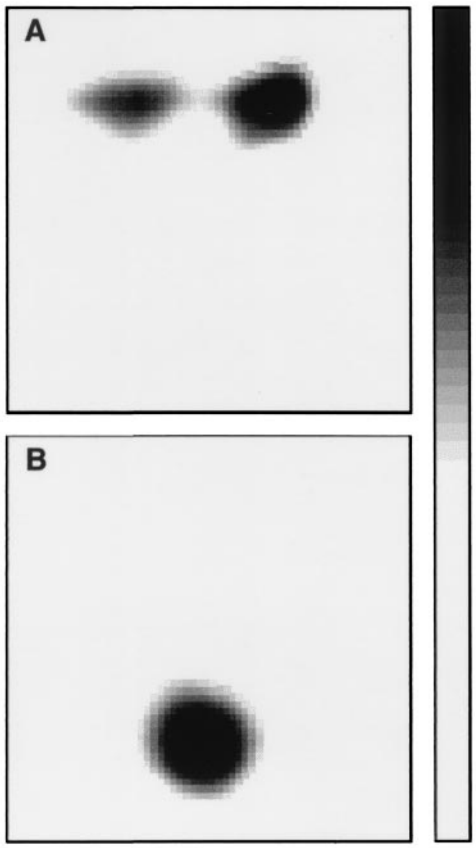

FIGURE 7 Separative-ESR-CT images of DMPO-OH (*A*) and Fe^{2+}-MGD-NO (*B*). Each image (30 mm × 30 mm range) was reconstructed with six spatial projections at different spatial axes, as shown with P_B for DMPO-OH and $P_A - P_B$ for Fe^{2+}-MGD-NO in Fig. 5. Intensities of DMPO-OH among the spatial functions were calibrated to the initial signal intensity from Fig. 6. The scale and position of the square were fitted to those shown in Fig. 4 *D*.

In the former, an equal correction is added to each pixel in the ray, and in the latter, the correction is influenced by the present density of the pixels. As the result, the additive correction shows tailing artifacts in the direction of the final correction, while the multiplicative correction markedly reinforces spike noise. Spike noise is often observed in the spectra of L-band ESR spectroscopy. We therefore improved an existing ART algorithm by modifying the additive correction with pixel density and area, using the following equation: $i_{m,n,k+1} = i_{m,n,k} + (p_j - p'_j) \times i_{m,n,k} \times w_{m,n,j}/p'_j$; where p_j and p'_j are the intensities of the *j*th observed and calculated projections, respectively; $i_{m,n,k}$ is the density of the pixel (m, n) at the *k*th iteration; and $w_{m,n,j}$ is the weighting factor of the pixel (m, n) toward the *j*th projection. Use of only a single iteration of mART after FBP reconstruction gave a satisfactory image with no remarkable tailing artifacts and no spike noise. Because of the decrease in tailing and spike noise, the accuracy of spatial projection of the individual radical was increased. In this experiment, the resolution of the final 2D spatial image was affected more by the maximum field gradient than by the projection number and was below 5 mm, even though only four projections were used for the reconstruction. More than 12 projections were required to obtain a similar resolution by FBP reconstruction only.

This separable ESR-CT technique was combined with spin trapping and L-band ESR spectroscopy, resulting in the first successful simultaneous separative imaging of ·NO and ·OH. Most spin adducts of DMPO with oxygen radicals such as ·OH and/or $\cdot O_2^-$ are unstable, and the half-life of DMPO-OH has been reported to be ~50 s (Rouband et al., 1997) or even shorter in living cells (Sentjurc et al., 1995). The ESR signal of the spin adducts disappeared during long data acquisition times. Therefore, we improved the algorithm by calibrating the signal intensity to the initial one. This improvement should be widely applicable, because in vivo spin adducts of different radical species have different signal decay rates.

The spin trapping technique for using Fe^{2+}-carbamate complex has been successfully applied to in vivo detection (Komarov et al., 1993, Lai and Komarov, 1994; Quaresima et al., 1996) and imaging (Yokoyama et al., 1997) of ·NO. Previous in vivo spin trappings of reactive oxygen species have not been successful, although Liu et al. (1999) recently reported a more stable spin trapping agent. The combination of the separable ESR-CT technique with more stable spin trapping reagents would make it possible to determine not only the amount but also the location of these radical formations in vivo.

In this technique, no preliminary knowledge is required with regard to ESR components. And imaging reconstruction is possible even when the spectral separation in 2D spectral-spatial imaging is insufficient, provided the characteristics of the spectrum may be found in the 2D spectral-spatial imaging. Indeed, we succeeded in the separative imaging of free and liposomal spin probes (data not shown). The present results strongly suggest that this technique would be further applicable to in vivo investigation of other free radical reactions. This separable ESR-CT imaging technique might become one of the most powerful diagnosis techniques.

This work was supported by a Grant-in-Aid for Developmental Scientific Research, a Grant-in-Aid for General Scientific Research, and Takeda Research Foundation.

REFERENCES

Akaike, T., M. Yoshida, Y. Miyamoto, K. Sato, M. Kohno, K. Sasamoto, K. Miyazaki, S. Ueda, and H. Maeda. 1993. Antagonistic action of imidazolineoxyl N-oxides against endothelium-derived relaxing factor/·NO through a radical reaction. *Biochemistry.* 32:827–832.

Alecci, M., S. Colacicchi, P. L. Indovina, F. Momo, P. Pavone, and A. Sotgiu. 1990. Three-dimensional in vivo ESR imaging in rats. *Magn. Reson. Imaging.* 8:59–63.

Berliner, L. J., and X. Wan. 1989. In vivo pharmacokinetics by electron magnetic resonance spectroscopy. *Magn. Reson. Med.* 9:430–434.

Bernardo, M. L., Jr., P. C. Lauterbur, and L. K. Hedges. 1985. Experimental example of NMR spectroscopic imaging by projection reconstruction involving an intrinsic frequency dimension. *J. Magn. Reson.* 61: 168–174.

Brooks, R. A., and G. D. Chiro. 1975. Theory of image reconstruction in computed tomography. *Radiology.* 117:561–572.

Eaton, S. S., M. M. Maltempo, E. D. A. Stemp, and G. R. Eaton. 1987. Three-dimensional EPR imaging with one spectral and two spatial dimensions. *Chem. Phys. Lett.* 142:567–569.

Ewert, U., and T. Herrling. 1986. Spectrally resolved EPR tomography with stationary gradient. *Chem. Phys. Lett.* 129:516–521.

Filep, J. G., C. Lapierre, S. Lachance, and J. S. Chan. 1997. Nitric oxide co-operates with hydrogen peroxide in inducing DNA fragmentation and cell lysis in murine lymphoma cells. *Biochem. J.* 321:897–901.

Gomi, F., H. Utsumi, A. Hamada, and M. Matsuo. 1993. Aging retards spin clearance from mouse brain and food restriction prevents its age-dependent retardation. *Life Sci.* 52:2027–2033.

Gordon, R., R. Bender, and G. T. Herman. 1970. Algebraic reconstruction techniques (ART) for three-dimensional electron microscopy and x-ray photography. *J. Theor. Biol.* 29:471–481.

Gordon, R., and G. T. Herman. 1974. Three-dimensional reconstruction from projections: a review of algorithms. *Int. Rev. Cytol.* 38:111–151.

Herrling, T., N. Klimes, W. Karthe, U. Ewert, and B. Ebert. 1982. EPR zeugmatography with modulated magnetic field gradient. *J. Magn. Reson.* 49:203–211.

Hoch, M. J. R. 1981. Electron spin resonance imaging of paramagnetic centres in solids. *J. Phys. C Solid State Phys.* 14:5659–5666.

Ishida, S., S. Matsumoto, H. Yokoyama, N. Mori, H. Kumashiro, N. Tsuchihashi, T. Ogata, M. Yamada, M. Ono, T. Kitajima, H. Kamada, and E. Yoshida. 1992. An ESR-CT imaging of the head of a living rat receiving an administration of a nitroxide radical. *Magn. Reson. Imaging.* 10:109–114.

Katsuda, H., T. Kobayashi, H. Saito, T. Matsunaga, and M. Ikeya. 1990. Electron spin resonance imaging of mouse B16 melanoma. *Chem. Pharm. Bull.* 38:2838–2840.

Komarov, A., D. M. Mattson, M. Jones, P. K. Singh, and C. S. Lai. 1993. In vivo spin trapping of nitric oxide in mice. *Biochem. Biophys. Res. Commun.* 195:1191–1198.

Kuppusamy, P., M. Chzhan, A. Samouilov, P. Wang, and J. L. Zweier. 1995. Mapping the spin-density and lineshape distribution of free radicals using 4D spectral-spatial EPR imaging. *J. Magn. Reson. B.* 107: 116–125.

Kuppusamy, P., M. Chzhan, K. Vij, M. Shteynbuk, D. J. Lefer, E. Giannella, and J. L. Zweier. 1994. Three-dimensional spectral-spatial EPR imaging of free radicals in the heart: a technique for imaging tissue metabolism and oxygenation. *Proc. Natl. Acad. Sci. USA.* 91: 3388–3392.

Kuppusamy, P., and J. L. Zweier. 1995. EPR imaging of free radicals in the perfused heart. *Curr. Top. Biophys.* 18:3–13.

Lai, C. S., and A. M. Komarov. 1994. Spin trapping of nitric oxide produced in vivo in septic-shock mice. *FEBS Lett.* 345:120–124.

Lauterbur, P. C., D. N. Levin, and R. B. Marr. 1984. Theory and simulation of NMR spectroscopic imaging and field plotting by projection reconstruction involving an intrinsic frequency dimension. *J. Magn. Reson.* 59:536–541.

Liu, K. J., M. Miyake, T. Panz, and H. M. Swartz. 1999. Evaluation of DEMPO as a spin trapping agent in biological system. *Free Radic. Biol. Med.* 26:714–721.

Maltempo, M. M. 1986. Differentiation of spectral and spatial components in EPR imaging using 2-D image reconstruction algorithms. *J. Magn. Reson.* 69:156–161.

Maltempo, M. M., S. S. Eaton, and G. R. Eaton. 1987. Spectral-spatial two-dimensional EPR imaging. *J. Magn. Reson.* 72:449–455.

Maltempo, M. M., S. S. Eaton, and G. R. Eaton. 1988. Reconstruction of spectral-spatial two-dimensional EPR images from incomplete sets of projections without prior knowledge of the component spectra. *J. Magn. Reson.* 77:75–83.

Maltempo, M. M., S. S. Eaton, and G. R. Eaton. 1991. Algorithms for spectral-spatial imaging with a "missing angle." *In* EPR Imaging and In Vivo EPR. G. R. Eaton, S. S. Eaton, and K. Ohno, editors. CRC Press, Boca Raton, FL. 145–152.

Masuda, S., H. Utsumi, and A. Hamada. 1992. In vivo ESR studies on radical reaction in ischemia paw edema of whole mouse. *In* Oxygen Radicals. K. Yagi, M. Kondo, E. Niki, and T. Yoshikawa, editors. Elsevier Science Publishers, Amsterdam. 175–178.

Matsumoto, K., K. Endo, and H. Utsumi. 2000. In vivo electron spin resonance assessment of decay constant of nitroxyl radical in selenium-deficient rat. *Biol. Pharm. Bull.* 23:641–644.

Miura, Y., A. Hamada, and H. Utsumi. 1995. In vivo ESR studies of antioxidant activity on free radical reaction in living mice under oxidative stress. *Free Radic. Res.* 22:209–214.

Miura, Y., H. Utsumi. and A. Hamada. 1992. Effect of inspired oxygen concentration of in vivo redox reaction of nitroxide radicals in whole mice. *Biochem. Biophys. Res. Commun.* 182:1108–1114.

Ohno, K. 1982. ESR imaging: a deconvolution method for hyperfine patterns. *J. Magn. Reson.* 50:145–150.

Quaresima, V., H. Takehara, K. Tsushima, M. Ferrari, and H. Utsumi. 1996. In vivo detection of mouse liver nitric oxide generation by spin trapping electron paramagnetic resonance spectroscopy. *Biochem. Biophys. Res. Commun.* 221:729–734.

Phumala, N., T. Ide, and H. Utsumi. 1999. Noninvasive evaluation of in vivo free radical reactions catalyzed by iron using in vivo ESR spectroscopy. *Free Radic. Biol. Med.* 26:1209–1217.

Rouband, V., S. Sankarapandi, P. Kuppusamy, P. Tordo, and J. L. Zweier. 1997. Quantitative measurement of superoxide generation using the spin trap 5-(diethoxyphosphoryl)-5-methyl-1-pyrroline-*N*-oxide. *Anal. Biochem.* 247:404–411.

Sandau, K., J. Pfeilschifter, and B. Brune. 1997. The balance between nitric oxide and superoxide determines apoptotic and necrotic death of rat mesangial cells. *J. Immunol.* 158:4938–4946.

Sano, H., K. Matsumoto, and H. Utsumi. 1997. Synthesis and imaging of blood-barrier permeable nitroxyl-probes for free radical reactions in brain of living mice. *Biochem. Mol. Biol. Int.* 42:641–647.

Sano, H., M. Naruse, K. Matsumoto, T. Oi, and H. Utsumi. 2000. A new nitroxyl-probe with high retentivity in brain and its application to brain imaging. *Free Radic. Biol. Med.* 28:959–969.

Sano, T., F. Umeda, T. Hashimoto, H. Nawata, and H. Utsumi. 1998. Oxidative stress measurement by in vivo electron spin resonance spectroscopy in rats with streptozotocin-induced diabetes. *Diabetologia.* 41:1355–1360.

Sentjurc, M., H. M. Swartz, and N. Kocherginsky. 1995. Metabolism, toxicity, and distribution of spin trap. *In* Nitroxide Spin Labels: Reaction Is Biology and Chemistry. N. Kocherginsky and M. Swartz, editors. CRC Press, Boca Raton, FL.199–206.

Shepp, L. A., and B. F. Logan. 1974. The Fourier reconstruction of a head section. *IEEE Trans. Nucl. Sci.* NS21:21–43.

Sinobu, L. A., S. G. Jones, and M. M. Jones. 1984. Sodium *N*-methyl-D-glucamine dithiocarbamate and cadmium intoxication. *Acta Pharmacol. Toxicol.* 54:189–194.

Sotgiu, A., D. Gazzillo, and F. Momo. 1987. ESR imaging: spatial deconvolution in the presence of an asymmetric hyperfine structure. *J. Phys. C Solid State Phys.* 20:6297–6304.

Sueki, M., G. R. Eaton, and S. S. Eaton. 1990. Electron spin echo and CW perspectives in 3D EPR imaging. *Appl. Magn. Reson.* 1:20–28.

Takeshita, K., A. Hamada, and H. Utsumi. 1999. Mechanisms related to reduction of radical in mouse lung using an L-band ESR spectrometer. *Free Radic. Biol. Med.* 26:951–960.

Takeshita, K., H. Utsumi, and A. Hamada. 1991. ESR measurement of radical clearance in lung of whole mouse. *Biochem. Biophys. Res. Commun.* 177:874–880.

Takeshita, K., H. Utsumi, and A. Hamada. 1993. Whole mouse measurement of paramagnetism-loss of nitroxide free radical in lung with an L-band ESR spectrometer. *Biochem. Mol. Biol. Int.* 29:17–24.

Utsumi, H., E. Muto, S. Masuda, and A. Hamada. 1990. In vivo ESR measurement of free radicals in whole mice. *Biochem. Biophys. Res. Commun.* 172:1342–1348.

Utsumi, H., K. Takeshita, Y. Miura, S. Masuda, and A. Hamada. 1993. In vivo EPR measurement of radical reaction in whole mice: Influence of inspired oxygen and ischemia-reperfusion injury on nitroxide reduction. *Free Radic. Res. Commun.* 19:S219–S225.

Woods, R. K., W. B. Hyslop, R. B. Marr, and P. C. Lauterbur. 1991. Image reconstruction. *In* EPR Imaging and In Vivo EPR. G. R. Eaton, S. S. Eaton, and K. Ohno, editors. CRC Press, Boca Raton, FL. 91–117.

Xie, Y. W., and M. S. Wolin. 1996. Role of nitric oxide and its interaction with superoxide in the suppression of cardiac muscle mitochondrial respiration. Involvement in response to hypoxia/reoxygenation. *Circulation.* 94:2580–2586.

Yokoyama, H., S. Fujii, T. Yoshimura, H. Ohya-Nishiguchi, and H. Kamada. 1997. In vivo ESR-CT imaging of the liver in mice receiving subcutaneous injection of nitric oxide-bound iron complex. *Magn. Reson. Imaging.* 15:249–253.

Yoshie, Y., and H. Ohshima. 1997. Nitric oxide synergistically enhances DNA strand breakage induced by polyhydroxyaromatic compounds, but inhibits that induced by the Fenton reaction. *Arch. Biochem. Biophys.* 342:13–21.